RSC Advances

PAPER

View Article Online
View Journal | View Issue

Cite this: *RSC Adv.*, 2017, **7**, 50358

Spontaneously grown $Ni(OH)_2$ on iron oxide nanoparticles with enhanced energy storage performance for electrodes of asymmetric supercapacitors†

Yue Wang,[ab] Xianfeng Zhang,[a] Xin Li,[a] Yang Liu,[a] Xiaoping Wang,[c] Xi Liu,[c] Jian Xu,[c] Yongwang Li,[c] Yongguang Liu,[a] Hang Wei,[a] Peng Jiang *[ab] and Minghui Liang *[a]

Iron oxide nanoparticles intercalated in $Ni(OH)_2$ nanosheets were prepared in a spontaneous way for the cathode materials of asymmetric supercapacitors. The soluble precursor of $Ni(OH)_2$, $Ni(NH_3)_6(OH)_2$, was used for growth on α-Fe_2O_3 nanoparticles. The loading percentages of $Ni(OH)_2$ in the $Ni(OH)_2$–α-Fe_2O_3 nanocomposites had a great influence on the morphology and size of $Ni(OH)_2$. The composites were characterized by TEM, SEM, ICP-OES, XRD and XPS. The specific capacitance of $Ni(OH)_2$ in the composite can reach 1107 F g^{-1} at a scan rate of 20 mV s^{-1}, and the specific capacitance of the $Ni(OH)_2$–α-Fe_2O_3 composite can be up to 376 F g^{-1} at a scan rate of 5 mV s^{-1}. More importantly, the fabricated $Ni(OH)_2$–α-Fe_2O_3//AC (activated carbon) asymmetric supercapacitor exhibited energy density and power density of 31.6 W h Kg^{-1} and 474 W Kg^{-1}, respectively. The cycling performance of the asymmetric supercapacitor was also excellent, and the capacitance retention reached 89.6% after 5000 charge–discharge cycles. Red, blue and yellow LED lights can be lit up with two series of asymmetric supercapacitors, revealing their potential application in energy storage.

Received 17th August 2017
Accepted 13th October 2017

DOI: 10.1039/c7ra09119b

rsc.li/rsc-advances

1. Introduction

Electrochemical energy is not only an important alternative energy source for fossil fuels but a requisite element in the portable electronic devices, such as cell phones and wearable electronic devices.[1–4] Supercapacitors are a kind of energy storage device being able to deliver electric energy in a fast way, but they suffer from relatively low energy densities.[5,6] The energy densities of supercapacitors are of positive correlation to their specific capacitances and the square of their operating voltages.[7] Therefore, there are two ways to improve the energy densities of supercapacitors. One is to improve the specific capacitance of supercapacitors. And another is to enlarge the potential range of the supercapacitors.

Metal oxides/hydroxides, such as MnO_2,[8,9] NiO/$Ni(OH)_2$,[10,11] and RuO_2,[12,13] have high specific capacitances, thus they are promising choice for high energy density supercapacitors. In particular, $Ni(OH)_2$ not only has high theoretical specific capacitance, but is a cheap and environment-friendly material, thus it has been intensively investigated for the electrode of supercapacitors.[14–17] Recently, we reported the preparation and superior energy storage performance of ultra-fine $Ni(OH)_2$ particles supported on carbon materials.[18] In that work, soluble precursor of $Ni(OH)_2$, *i.e.* $Ni(NH_3)_6(OH)_2$, is used to grow $Ni(OH)_2$ material over carbon materials. However, one drawback for this route is that the superior performance can only be obtained at low loading percentages of $Ni(OH)_2$. The apparent specific capacitance of $Ni(OH)_2$/C materials at low loading percentages of $Ni(OH)_2$ is relatively low. On the other hand, the symmetric supercapacitors based on $Ni(OH)_2$ often have relatively low operating voltages, limiting the energy densities of the supercapacitors.

Asymmetric supercapacitors as one kind of supercapacitors have two dissimilar electrodes, including a battery-type faradic electrode (cathode) as an energy source and a capacitor-type electrode (anode) as a power source.[14,19] Asymmetric supercapacitors have wide electrochemical window because of two different electrodes, and thus they have comparable energy densities with batteries and lithium ions batteries.[20,21] The cathode materials for asymmetric supercapacitors include metal oxides/hydroxides, and the anode materials are often carbon materials.[22] As a result of higher theoretical specific capacitance of cathode materials than that of anode materials, to improve the practical specific capacitance of cathode

[a]CAS Center for Excellence in Nanoscience, Key Laboratory of Nanosystem and Hierarchical Fabrication, National Center for Nanoscience and Technology (NCNST), Beijing 100190, P. R. China. E-mail: pjiang@nanoctr.cn; liangmh@nanoctr.cn

[b]University of Chinese Academy of Sciences, Beijing 100049, P. R. China

[c]Synfuels China Technology, Co. Ltd., Beijing 101400, P. R. China

† Electronic supplementary information (ESI) available: TEM images, XPS spectra, CV curves, BET data, and GCD curves. See DOI: 10.1039/c7ra09119b

materials is an important issue for enhancing the performance of asymmetric supercapacitors.[23]

To apply $Ni(OH)_2$-based materials prepared from soluble $Ni(NH_3)_6(OH)_2$ in asymmetric supercapacitors, the support materials other than carbon materials are desired to be tried. Iron oxides are not only active for electrochemical energy storage, but stable in alkaline or neutral solution.[24–28] On the other hand, iron oxides have higher conductivity than that of $Ni(OH)_2$, leading to better charge transfer than pure $Ni(OH)_2$.[29,30] Therefore, iron oxides are the promising candidates for the support of $Ni(OH)_2$ material. The composites of Fe_2O_3 and $Ni(OH)_2$ for the electrode of supercapacitors have been reported.[31–33] However, the composites are prepared with solvothermal methods.[29,34,35] With such route, it is difficult to controllably prepare $Ni(OH)_2$ with desired morphology and size, which are important factors influencing the energy storage performance of $Ni(OH)_2$. It is highly desirable to develop a route to controllably prepare $Ni(OH)_2$ based materials with desired morphology and size. The rule of soluble $Ni(NH_3)_6(OH)_2$ growing on the iron oxide is unknown, being worthy exploring in the viewpoint of nanocomposites preparation. Furthermore, the asymmetric supercapacitors based on $Ni(OH)_2$–α-Fe_2O_3 composites have not been reported, to the best of our knowledge.

Based on above problems, herein, we report the spontaneous growth of $Ni(OH)_2$ on α-Fe_2O_3 and the electrochemical energy storage performance of the asymmetric performance based on $Ni(OH)_2$–α-Fe_2O_3 cathode and active carbon anode. The growth behaviors of $Ni(OH)_2$ on α-Fe_2O_3 with different loading percentages are also investigated.

2. Experimental

2.1 Reagents

All the chemicals are of analytical grade and used without further purification. NaCl (99.5%), NaOH (96%) were purchased from Sinopharm Chemical Reagents Co. Ltd. $FeCl_3 \cdot 6H_2O$ (99%), Acetylene Black, PVDF were supplied by Aladdin Reagents Co. Ltd. $NiCl_2 \cdot 6H_2O$ (≥98.0%) was obtained from Tianjin Guangfu Technology Development Co. Ltd. $NH_3 \cdot H_2O$ (25–28%), HNO_3 (65.0–68.0%), H_2SO_4 (95–98%) and DMF were provided by Beijing Chemical Reagents Co. Ltd. The carbon cloth (WOS 1002) was purchased from Ce Tech Co. Ltd.

2.2 Material preparation

2.2.1 Preparation of α-Fe_2O_3 nanoparticles. The α-Fe_2O_3 nanoparticles were prepared according to the procedures previously reported, with some modifications.[36–38] In a typical experiment, ammonia aqueous solution (10 wt%) was added into 100 mL $FeCl_3$ aqueous solution (4 wt%) to adjust the pH to about 7.5, and a red precipitate could be observed. The precipitate was separated by centrifugation, washed with water, and peptized in 30 mL of aqueous solution of $FeCl_3$ (1.2 wt%), and then a transparent colloidal solution of ferric hydroxide can be obtained. Nanosized ferric hydroxide particles were obtained by adding saturated NaCl aqueous solution to the colloidal solution and freeze-drying the produced sediment with a freeze drier. The α-Fe_2O_3 nanoparticles can be obtained through annealing the ferric hydroxide particles at 550 °C for 3 hours in air and washing the powder with water to remove residue NaCl.

2.2.2 Preparation of $Ni(OH)_2$/α-Fe_2O_3 nanocomposite. The $Ni(NH_3)_6(OH)_2$ was used as the precursor for the active electrode material $Ni(OH)_2$, which was prepared as reported previously.[18,39] In brief, $Ni(OH)_2$ being obtained by chemical precipitation method was dissolved in ammonia aqueous solution (28 wt%) to form $Ni(NH_3)_6(OH)_2$. The calculated amount of α-Fe_2O_3 nanoparticles was dispersed in the $Ni(NH_3)_6(OH)_2$ solution, and the $Ni(OH)_2$–α-Fe_2O_3 composite with desired loading percentages can be obtained by evaporating all of the liquid at 353 K under stirring condition.

2.2.3 Preparation of electrodes. The carbon cloth (CC) was used as current collector, which had been treated by mixed acid (H_2SO_4–HNO_3 ratio 3 : 1) at 333 K for 2 h and then washed by ethanol, acetone and DI water, respectively before use. The active material (80 wt%), acetylene black (10 wt%) as conductive additive, and PVDF (10 wt%) as binder were mixed with DMF to form slurry. The mixed slurry was coated onto the pretreated CC following drying treatment, and the loading mass of the active material was about 2 mg cm^{-2}.

2.3 Material characterizations

Scanning electron microscopy (SEM) images were collected on NOVA Nano SEM 430; transmission electron microscopy (TEM) images and HRTEM images were obtained on Tecnai G2 F20 U-TWIN. The X-ray diffraction (XRD) measurements were performed on an X-ray diffractometer (XRD, Rigaku, D/MAX-TTRIII, 200 kV, 40 mA) with Cu Kα radiation (λ = 0.154178 nm). The loading percentages of $Ni(OH)_2$ on the $Ni(OH)_2$–α-Fe_2O_3 were obtained by an inductively coupled plasma atomic emission spectroscopy (ICP-OES, Optima 8300). The chemical valence state and composition of the samples were measured on the X-ray photoelectron spectroscopy spectra (XPS, ESCALAB250Xi). The BET data were obtained on ASAP 2020 (Micrometrics). The elemental mapping images were collected on Talos™ 200A.

2.4 Electrochemical measurements

The electrochemical measurements of the $Ni(OH)_2$–α-Fe_2O_3 composite electrodes were performed on an electrochemical workstation (CHI 660D) in a standard three-electrode cell. The $Ni(OH)_2$–α-Fe_2O_3 on the CC substrate (1 cm × 2 cm), a Ag/AgCl electrode (with saturated KCl solution), and a platinum foil (2 cm × 4 cm) were used as the working, reference and counter electrode, respectively. All the electrochemical measurements were executed in 1 M KOH aqueous electrolyte. The distance between working electrode and counter electrode was about 2.0 cm. The cyclic voltammograms (CVs) were measured between 0 and 0.6 V at the scan rates from 5 to 80 mV s^{-1}. The galvanostatic charging/discharging (GCD) curves were collected between 0 and 0.45 V at the current densities from 2 to 20 A g^{-1}. The electrochemical impedance spectroscopy (EIS) was obtained by applying an AC voltage of 5 mV amplitude in the frequency from 0.01 Hz to 10 kHz. The specific capacitances of

the composite and α-Fe_2O_3 were calculated from CV and galvanostatic charge/discharge curves according to the following two equations,[40] respectively:

$$C = \frac{\int_a^b I(V)\mathrm{d}V}{2\Delta V v m} \quad (1)$$

$$C = \frac{I\Delta t}{m\Delta V} \quad (2)$$

where $\int_a^b I(V)\mathrm{d}V$ is the integrated area of CV curve in one cycle, ΔV is the voltage window, v is the scan rate, I is the constant discharge current, Δt is the discharging time, and m is the mass of the $Ni(OH)_2$ or $Ni(OH)_2$–α-Fe_2O_3.

The asymmetric supercapacitors based on AC/CC and $Ni(OH)_2$–α-Fe_2O_3/CC were fabricated in 1 M KOH aqueous solution. The specific capacitances of the symmetric supercapacitors were calculated from CV and galvanostatic charge/discharge curves according to the following two equations, respectively:

$$C = \frac{2\int_a^b I(V)\mathrm{d}V}{\Delta V v(m_1 + m_2)} \quad (3)$$

$$C = \frac{4\ I\Delta t}{(m_1 + m_2)\Delta V} \quad (4)$$

where $\int_a^b I(V)\mathrm{d}V$ is the integrated area of CV curve in one cycle, ΔV is the voltage window, v is the scan rate, I is the constant discharge current, Δt is the discharging time, and m_1 and m_2 are the masses of double electrodes, *i.e.* $Ni(OH)_2$–α-Fe_2O_3 or AC.

3. Results and discussion

$Ni(NH_3)_6(OH)_2$ is a soluble precursor for $Ni(OH)_2$.[41,42] After the evaporation of NH_3 and water, $Ni(OH)_2$ can be spontaneously produced. Based on this mechanism, the $Ni(OH)_2$–α-Fe_2O_3 nanocomposites with different loading percentages of $Ni(OH)_2$ can be prepared according to Scheme 1. With low loading percentages of $Ni(OH)_2$, the ultra-small $Ni(OH)_2$ nanoparticles on the surface of α-Fe_2O_3 particles can be obtained as we have proved in our previous work; with high loading percentages of $Ni(OH)_2$, the α-Fe_2O_3 nanoparticles were intercalated in the $Ni(OH)_2$ nanosheets. The percentages of $Ni(OH)_2$ in the $Ni(OH)_2$–α-Fe_2O_3 nanocomposites measured by ICP-OES were listed in Table 1. According to the desired percentages of $Ni(OH)_2$, the samples were denoted as *X*-NF (*X* is the desired percentage plus 100; for example, 20-NF for 20 wt% $Ni(OH)_2$–α-Fe_2O_3 composite).

Fig. 1 shows the scanning electron microscopy (SEM) images of the pure α-Fe_2O_3 sample and $Ni(OH)_2$–α-Fe_2O_3 nanocomposites with different loading amounts of $Ni(OH)_2$. When the loading percentages of $Ni(OH)_2$ were lower than 10%, the $Ni(OH)_2$ aggregates cannot be observed in the SEM images. As the loading percentage reached 10%, the $Ni(OH)_2$ nanosheets can be observed. The loading percentages of $Ni(OH)_2$ further increased, the thickness and the amount of $Ni(OH)_2$ nanosheets

Table 1 The percentages of $Ni(OH)_2$ in the $Ni(OH)_2$–α-Fe_2O_3 composites

Sample	Fe_2O_3	5-NF	10-NF	20-NF	50-NF
Desired percentage	0	5%	10%	20%	50%
Measured percentage	0.01%	5.35%	11.57%	22.88%	48.97%

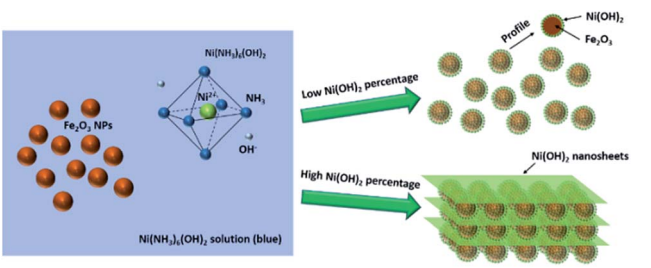

Scheme 1 Schematic illustration for the preparation of $Ni(OH)_2$–α-Fe_2O_3 nanocomposites.

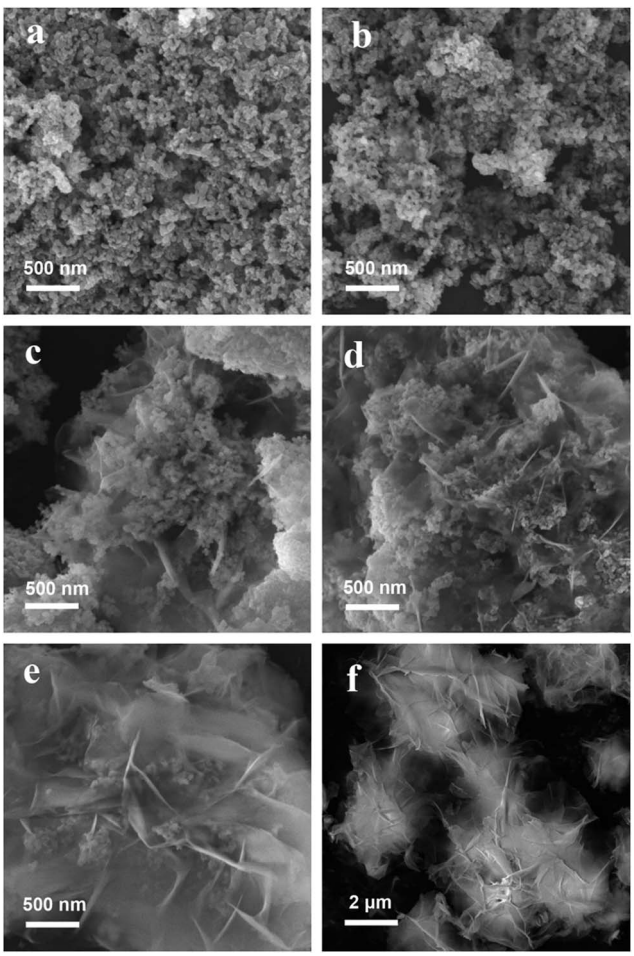

Fig. 1 The SEM images of (a) Fe_2O_3 and (b) 5-NF, (c) 10-NF, (d) 20-NF, (e) 50-NF, and (f) $Ni(OH)_2$.

increased. α-Fe_2O_3 nanoparticles were intercalated in the $Ni(OH)_2$ nanosheets for 20-NF and 50-NF as Scheme 1 depicted. The same phenomena can also be seen in the TEM images of these samples (Fig. S1†). Pure $Ni(OH)_2$ nanosheets can be obtained by evaporating all of the liquid of $Ni(NH_3)_6(OH)_2$ aqueous solution (Fig. 1f).

The TEM and HRTEM images of α-Fe_2O_3 nanoparticles, 20-NF and $Ni(OH)_2$ are shown in Fig. 2. The size of prepared α-Fe_2O_3 nanoparticles is about 10–30 nm. The crystalline lattice of α-Fe_2O_3 with a *d*-spacing distance of 0.369 nm can be clearly observed in the Fig. 2b, which can be attributed to the crystalline information of α-Fe_2O_3 (012).[43] The $Ni(OH)_2$ nanosheets in 20-NF and $Ni(OH)_2$ can be found in Fig. 2c and e, respectively. As seen from Fig. 2d and f, the crystalline lattice (0.336 nm) being able to attribute to $Ni(OH)_2$ (101) can be clearly observed for the sample 20-NF and $Ni(OH)_2$.

In our previous report, ultrafine $Ni(OH)_2$ particles grown on activated carbon can be observed with elemental mapping technique. To reveal the structure of $Ni(OH)_2$ grown on iron oxide with low loading percentages, the elemental mapping images of 10-NF were obtained (Fig. 3). Fig. 3a and b show the TEM image and STEM image of 10-NF for the same sample,

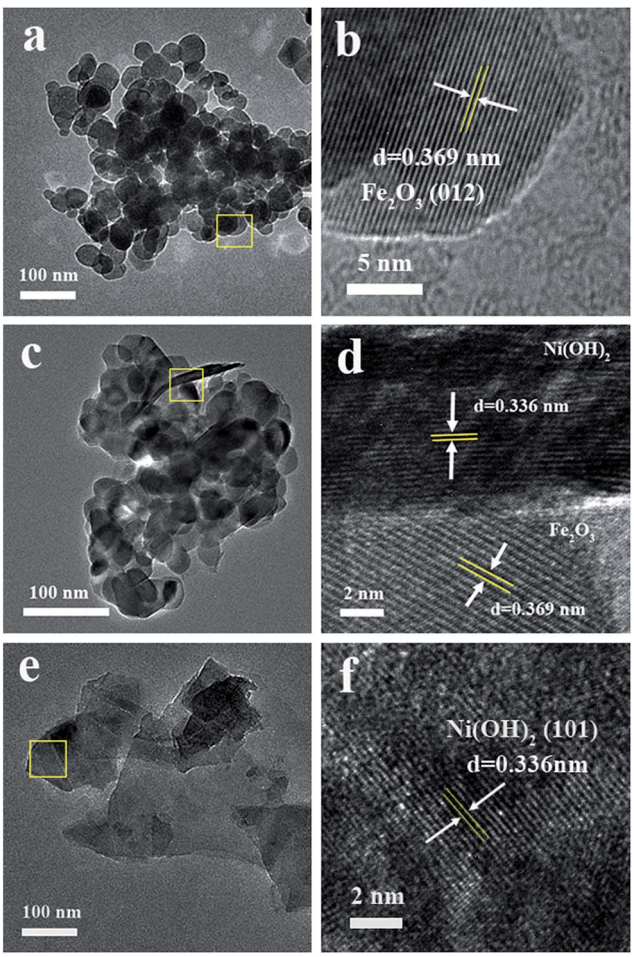

Fig. 2 (a) The TEM images and (b) the high resolution image of α-Fe_2O_3; (c) the TEM images and (d) the high resolution image of 20-NF; (e) the TEM images and (f) the high resolution image of $Ni(OH)_2$.

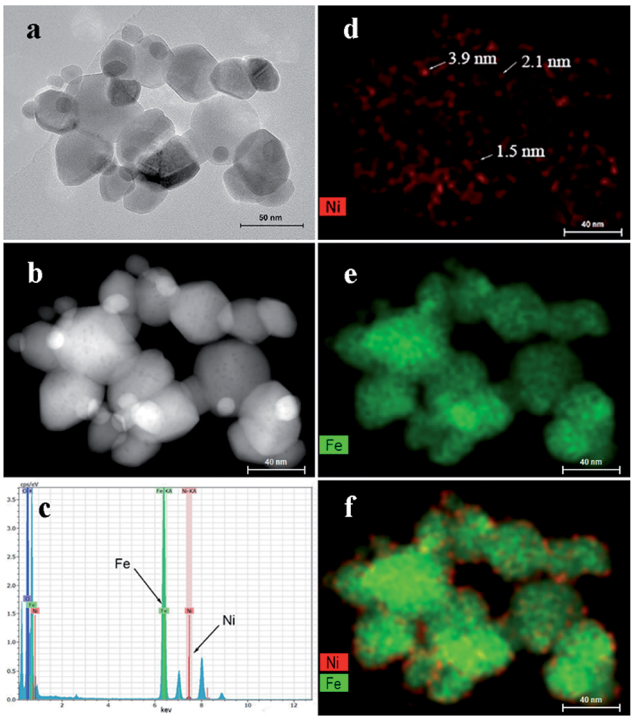

Fig. 3 (a) The TEM and (b) STEM images of 10-NF; (c) the EDS spectrum of 10-NF; the element mapping of (d) Ni, (e) Fe and (f) combined signals of Ni and Fe.

respectively. The $Ni(OH)_2$ nanosheets cannot be observed in this sample, even if the sample was observed at high resolution TEM images (Fig. S2†). However, the signals of Ni and Fe can be found in the EDS pattern (Fig. 3c), and the signal of Ni is weak. These results reveal the existence of nickel in the selected area. The elemental mapping results for Ni and Fe further prove the existence of Ni in the composite (Fig. 3d–f). The typical size of Ni in the composite is in the range of 1.5 to 3.9 nm, and Ni was evenly distributed on the surface of iron oxide according to the crystalline structure of iron oxide and Fig. 3f. It should be stated that the observed signal of Ni is the sum of the signal in the vertical way, so the actual size of Ni on the surface should be smaller than that we observed.

The XRD patterns of the prepared α-Fe_2O_3, 5-NF, 10-NF, 20-NF, 50-NF, and $Ni(OH)_2$ are shown in Fig. 4. The diffraction peaks for α-Fe_2O_3 (012), (104), (110) and $Ni(OH)_2$ (001), (100), (101) *etc.* can be indexed as JCPDS no. 33-0664 and no. 14-0117, respectively.[44–46] The loading percentage of $Ni(OH)_2$ being lower than 10 wt%, the diffraction signals of $Ni(OH)_2$ cannot be observed in the XRD patterns, which is consistent with the results of TEM, elemental mapping results and SEM. The signals of $Ni(OH)_2$ and α-Fe_2O_3 can be found in the XRD patterns for 20-NF and 50-NF, revealing $Ni(OH)_2$–α-Fe_2O_3 nanocomposites with high $Ni(OH)_2$ loading were composed of the crystalline $Ni(OH)_2$ nanosheets and α-Fe_2O_3 materials.

To know the specific surface area and porous structure of $Ni(OH)_2$–α-Fe_2O_3 nanocomposite, the adsorption and desorption isotherm curves of $Ni(OH)_2$, α-Fe_2O_3 and 50-NF were obtained as shown in Fig. S3.† The specific surface areas of

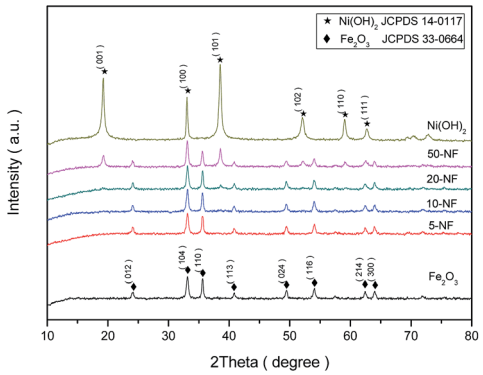

Fig. 4 XRD patterns of α-Fe_2O_3, 5-NF, 10-NF, 20-NF, 50-NF and $Ni(OH)_2$.

$Ni(OH)_2$, α-Fe_2O_3 and 50-NF were measured as 29.6, 27.6 and 32.8 $m^2\ g^{-1}$, respectively. The porous volumes of $Ni(OH)_2$, α-Fe_2O_3 and 50-NF were 0.036, 0.186 and 0.139 $cm^3\ g^{-1}$, respectively. The pore distribution of $Ni(OH)_2$, α-Fe_2O_3 and 50-NF are shown in the insets of Fig. S3.† There are little difference in their specific surface areas, and the pore volume of 50-NF is close to that of α-Fe_2O_3, so the synergistic effect between $Ni(OH)_2$ and α-Fe_2O_3 in electrochemical energy storage would be easily judged.

To reveal the chemical state of Ni and Fe in the $Ni(OH)_2$–α-Fe_2O_3 nanocomposite, the XPS (X-ray photoelectron spectroscopy) spectra of 20-NF were collected as shown in Fig. 5. The XPS survey spectrum of $Ni(OH)_2$–α-Fe_2O_3 reveals the presence of Ni, Fe, O (Fig. S4†). Two peaks in the Fe 2p XPS spectrum at about 711.07 and 724.67 eV (Fig. 5b) can be ascribed to Fe $2p^{3/2}$ and Fe $2p^{1/2}$ for α-Fe_2O_3, respectively.[47,48] The satellite peak centered at 719.62 eV is the characteristic signal of α-Fe_2O_3. The signals of iron in 20-NF are weaker than that in α-Fe_2O_3, indicating that the deposited $Ni(OH)_2$ on the surface of α-Fe_2O_3 reduced the exposed surface of α-Fe_2O_3. The binding energy of Ni in 20-NF was higher than that in $Ni(OH)_2$ for about 0.2 eV, indicating an electron transfer from $Ni(OH)_2$ to α-Fe_2O_3.

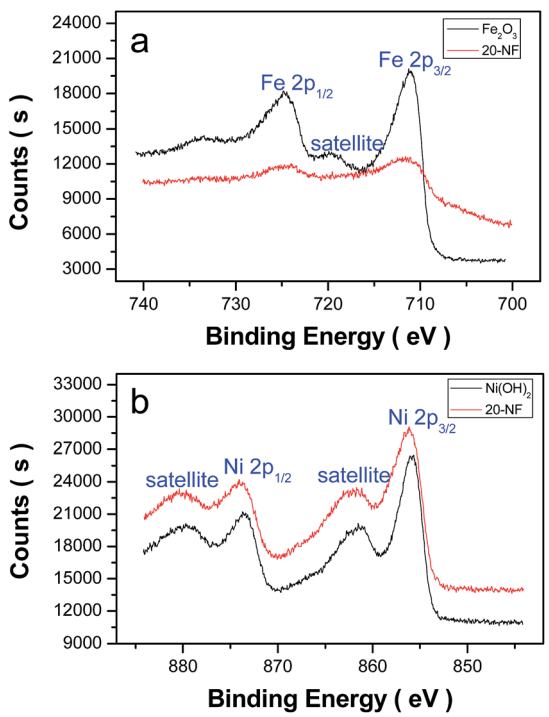

Fig. 5 XPS spectra of (a) Fe 2p for α-Fe_2O_3 and 20-NF, (b) Ni 2p for $Ni(OH)_2$ and 20-NF.

As the active materials in the working electrode, the energy storage performance of $Ni(OH)_2$/α-Fe_2O_3 nanocomposites was evaluated in a three-electrode system. Fig. 6a shows the CV curves of α-Fe_2O_3, 20-NF, 50-NF and $Ni(OH)_2$ at a scan rate of 20 mV s^{-1} under the voltage range of 0–0.6 V (*vs.* Ag/AgCl), and the CV curves of 5-NF and 10-NF are shown in Fig. S5.† A pair of redox peaks can be clearly observed over these samples, suggesting that the measured capacitance is mainly based on the pseudocapacitance derived from faradic processes.[17,49,50] The reaction process can be expressed as follows:

$$Ni(OH)_2 + OH^- \rightarrow NiOOH + H_2O + e^-$$

The influence of loading percentages for $Ni(OH)_2$ on the capacitance of the composites and $Ni(OH)_2$ is shown in Fig. 6b. We calculated the capacitive performance of the composites and $Ni(OH)_2$ according to the eqn (5) and (6):

$$C_{com} = C_{Fe_2O_3} \times P_{Fe_2O_3} + C_{Ni(OH)_2} \times P_{Ni(OH)_2} \quad (5)$$

$$C_{Ni(OH)_2} = (C_{com} - C_{Fe_2O_3} \times P_{Fe_2O_3})/P_{Ni(OH)_2} \quad (6)$$

where C_{com} is the specific capacitance of the composite $Ni(OH)_2/Fe_2O_3$, $C_{Fe_2O_3}$ is the specific capacitance of α-Fe_2O_3, $P_{Fe_2O_3}$ is the mass percentage of α-Fe_2O_3 in the composite, $C_{Ni(OH)_2}$ is the specific capacitance of $Ni(OH)_2$, and $P_{Ni(OH)_2}$ is the mass percentage of $Ni(OH)_2$ in the composite. The measured specific capacitances of α-Fe_2O_3, 5-NF, 10-NF, 20-NF, 50-NF and $Ni(OH)_2$ were 4.2, 37.1, 76.0, 158.5, 248.4 and 199 F g^{-1} at the scan rate of 20 mV s^{-1}. In the loading range of 5 to 20 wt% for $Ni(OH)_2$, the specific capacitance of the nanocomposites increased in a linear way with the increased loading of $Ni(OH)_2$, revealing the similar utilized efficiency of $Ni(OH)_2$ in these nanocomposites for electrochemical energy storage (Fig. 6b).

The calculated specific capacitances of $Ni(OH)_2$ in 20-NF can be up to 1107 F g^{-1} at a scan rate of 5 mV s^{-1}. However, as the loading percentages of $Ni(OH)_2$ reached 50 wt%, the utilized efficiency of $Ni(OH)_2$ for energy storage decreased to 507 F g^{-1}, which may be caused by the produced thick $Ni(OH)_2$ nanosheets in the composite. Interestingly, the specific capacitance of 50-NF was higher than that of $Ni(OH)_2$ and α-Fe_2O_3. The BET results revealed the similar specific surface areas for $Ni(OH)_2$, α-Fe_2O_3 and 50-NF, so a strong synergistic effect between α-Fe_2O_3 and $Ni(OH)_2$ nanosheets in NF composites can be concluded. The cyclic voltammetry (CV) curves of 50-NF and the specific capacitances for 50-NF and $Ni(OH)_2$ at the scanning rates from 5 to 80 mV s^{-1} are shown in Fig. 6c and d, respectively. The specific capacitance of 50-NF at the scan rate of 5 mV s^{-1} can reach 376 F g^{-1}. The calculated specific capacitances of $Ni(OH)_2$

in 50-NF were 768, 637, 507, 422, 306, and 213 F g^{-1} at scan rates of 5, 10, 20, 30, 50, and 80 mV s^{-1}, respectively. As the scan rate increased for 16 times (5 mV s^{-1} to 80 mV s^{-1}), the calculated specific capacitance of $Ni(OH)_2$ had a retention of 28%.

Furthermore, the GCD curves of the composites were collected to observe the charge–discharge behavior of the composites (Fig. 7a and S6†). Two steps involved for the charge–discharge process.[51] A fast charge step happened below 0.35 V and a slow charge step took place in the range of 0.35 to 0.45 V. The fast charge step maybe caused by capacitive charge, and during the slow step the faradic process happened. As the percentages of $Ni(OH)_2$ increased, the slow charge step experienced longer time. One possible reason is that increased amount of $Ni(OH)_2$ demanded longer time to complete the charge–discharge process. Another reason is that $Ni(OH)_2$ has worse conductivity than α-Fe_2O_3 and the composite with higher $Ni(OH)_2$ loading has lower conductivity.

To prove this point, EIS (electrochemical impedance spectroscopy) curves of the composites were obtained as shown in Fig. 7b. The EIS plots consist of a quasi-semicircle corresponding to the faradic reactions with the diameter representing the interfacial charge-transfer impedance (R_{ct}) at low frequency region, and a linear part representing the value of the internal resistance (R_s) at high frequency region.[52–54] The R_{ct} of α-Fe_2O_3, 20-NF, 50-NF and $Ni(OH)_2$ were calculated as 0.2 Ω, 0.43 Ω, 0.67 Ω, and 1.0 Ω, respectively. These results revealed that the increased loading percentages of $Ni(OH)_2$ led to higher resistance for charge transfer. This phenomenon may be caused by the lower conductivity of $Ni(OH)_2$ than α-Fe_2O_3. In the other viewpoint, the added α-Fe_2O_3 plays double roles: improving conductivity of the composite and acting as the intercalated substance in between $Ni(OH)_2$ nanosheets.

To investigate the potential for practical application of $Ni(OH)_2$–α-Fe_2O_3 materials, an asymmetric supercapacitor (ASC) was fabricated using the $Ni(OH)_2$–α-Fe_2O_3 composite as the positive electrode and AC as the negative electrode. The

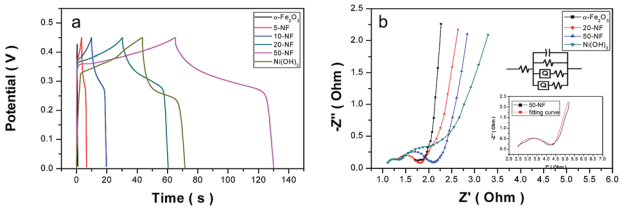

Fig. 7 (a) The GCD curves for the samples of Fe_2O_3, 5-NF, 10-NF, 20-NF, and 50-NF, at the current density of 4 A g^{-1} (based on the mass of Fe_2O_3 or $Ni(OH)_2$–α-Fe_2O_3); (b) the EIS spectra of Fe_2O_3, 20-NF, and 50-NF, the insets are the enlarged curves for 50-NF and equivalent circuit of 50-NF.

mass of the negative electrode (AC) was determined according to the charge balance theory.[40,55] The charge stored on each electrode was obtained from eqn (1) and (2).[56] Where C is specific capacitance, ΔV is the voltage range during charge–discharge test, and m is the mass of active material.

$$C = I \times t/\Delta V \times m \quad (7)$$

$$q = C \times \Delta V \times m \quad (8)$$

The charge balance follows the equation $q^+ = q^-$, we can get eqn (9):

$$m_+/m_- = C_- \times \Delta V_-/C_+ \times \Delta V_+ \quad (9)$$

where C_+ and C_- are the specific capacitances of 50-NF electrode and AC electrode, respectively, being obtained by the discharge curves (Fig. 8a). ΔV_+ and ΔV_- are the potential windows for cathode and anode, respectively. The optimal mass ratio between the $Ni(OH)_2$–α-Fe_2O_3 and AC electrodes is calculated to be $m_+/m_- \approx 0.26$ in the asymmetric supercapacitor.

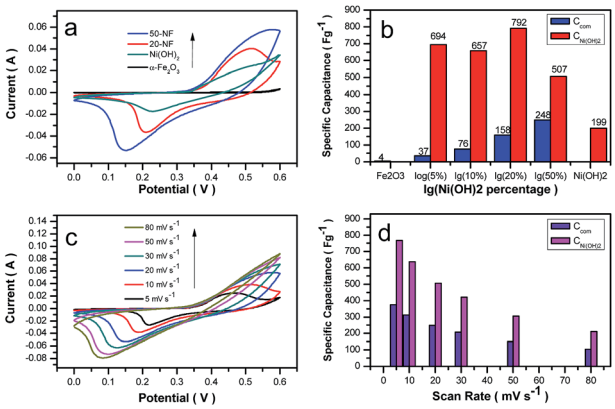

Fig. 6 (a) The CV curves of α-Fe_2O_3, 20-NF, and 50-NF, $Ni(OH)_2$, the scan rate was 20 mV s^{-1}; (b) the specific capacitances of composites and $Ni(OH)_2$ in $Ni(OH)_2$–α-Fe_2O_3 with different loading percentages of $Ni(OH)_2$; (c) the CV curves of 50-NF at different scan rates; (d) the dependence of calculated specific capacitances of composites and $Ni(OH)_2$ in 50-NF on the scan rates.

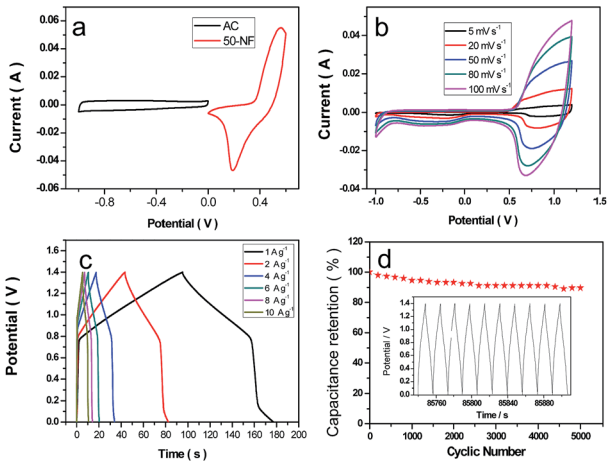

Fig. 8 Electrochemical characterizations of a symmetric supercapacitor based on 50-NF electrode (a) the CV curves at different potential window; (b) the CV curves at different scan rates; (c) the GCD curves of 20-NF at different current density; (d) the cycling performance for GCD at the current density of 4 A g^{-1}, and the inset is GCD curves of the last ten cycles.

Fig. 8b shows a series of CV curves of the asymmetric supercapacitor at various scan rates from 5 to 100 mV s^{-1} in a 1 M KOH aqueous electrolyte under the electrochemical window of −1.0–1.4 V. Furthermore, Fig. 8c shows the GCD curves of the asymmetric supercapacitor at different current densities under a potential window of 0–1.6 V. The energy density and power density of the symmetric supercapacitors were calculated from CV curves according to the following two equations, respectively:

$$E = 1/7.2CV^2 \quad (10)$$

$$P = 3600E/t \quad (11)$$

where E is the energy density, C is the capacitance calculated based on eqn (1) and (2), V is the voltage window, P is the power density, and t is the discharge time.

The $Ni(OH)_2/Fe_2O_3$//AC asymmetric supercapacitor cell exhibited high energy density and excellent power density of 31.6 W h Kg^{-1} and 474 W Kg^{-1} at a scan rate of 5 mV s^{-1}, 26.1 W h Kg^{-1} and 1567 W Kg^{-1} at 20 mV s^{-1}, 22.1 W h Kg^{-1} and 3308 W Kg^{-1} at 50 mV s^{-1}, 19.8 W h Kg^{-1} and 4748 W Kg^{-1} at 80 mV s^{-1}, 18.6 W h Kg^{-1} and 5578 W Kg^{-1} at 100 mV s^{-1}, respectively. When the power density of the asymmetric supercapacitor increased for more than 10 times, the retention of energy density can reach 59%. The cycling performance of $Ni(OH)_2$–α-Fe_2O_3//AC asymmetric supercapacitors is shown in Fig. 8d. After 5000 cycles, the capacitance retention rate was still 89.6%. To reveal the change of $Ni(OH)_2$–α-Fe_2O_3 after charge–discharge process, the TEM and SEM images for the cycled sample were obtained in Fig. S7.† However, there were not remarkable changes being able to be observed. The high capacitance retention maybe cause by the stable structure of $Ni(OH)_2$–α-Fe_2O_3 during charge–discharge process. The performance of our sample was compared with the reported concerning samples as listed in Table S1.† Our $Ni(OH)_2$–α-Fe_2O_3 sample has comparable performance with the reported electrodes. More importantly, the asymmetric capacitors based on $Ni(OH)_2$–α-Fe_2O_3 composite are reported by us for the first time.

Two series of $Ni(OH)_2$–α-Fe_2O_3//AC ASC devices charged by galvanostatic charging/discharging (GCD) techniques to 1.6 V can be used to drive different types of LED lights. Red LED light with a threshold voltage of 1.8 V, blue LED light with 2.6 V, and green LED with 2.9 V can be lighted up by the series devices, as shown in Fig. 9. More importantly, the charged ASC devices with 5 s charging time at a current density of 40 A g^{-1} can keep the red LED light lighting for 10 min.

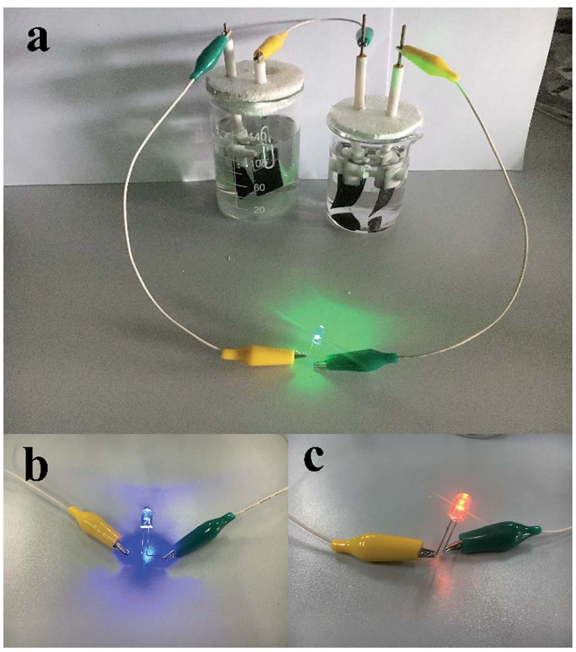

Fig. 9 The photographs of green LED (a), blue LED (b) and red LED (c) lights being lighted up by the series asymmetric supercapacitors.

4. Conclusions

In summary, we have developed a way to spontaneously grow $Ni(OH)_2$-based composites and investigate their electrochemical energy storage performance for asymmetric supercapacitors. Under low loading percentages of $Ni(OH)_2$ on α-Fe_2O_3, the ultrasmall $Ni(OH)_2$ particles form over α-Fe_2O_3 nanoparticles. The higher loading percentages of $Ni(OH)_2$ on α-Fe_2O_3 lead to the formation of the intercalated composites. Various characterization results including TEM, SEM, ICP-OES, XRD and XPS reveal the structure and composition of our composites. The energy storage performance of $Ni(OH)_2$–α-Fe_2O_3 composites is measured with CV method, and the specific capacitance of $Ni(OH)_2$–α-Fe_2O_3 composites increased with the increased $Ni(OH)_2$ loading. More interestingly, $Ni(OH)_2$–α-Fe_2O_3 composite with 50% $Ni(OH)_2$ loading exhibited higher specific capacitance that of $Ni(OH)_2$ and α-Fe_2O_3, revealing the strong synergistic effect between $Ni(OH)_2$ nanosheets and α-Fe_2O_3 nanoparticles. The fabricated asymmetric supercapacitor based on $Ni(OH)_2$–α-Fe_2O_3 and activated carbon exhibits the energy density and power density of 31.6 W h Kg^{-1} and 474 W Kg^{-1}. More importantly, even if the power density increased to 5578 W Kg^{-1}, the energy density still has 18.6 W h Kg^{-1}, implying their important application in high power devices. For practical application of the asymmetric supercapacitors, all kinds of LED lights can be lighted up by two series asymmetric supercapacitors. With 5 second charging time, the charged asymmetric supercapacitors can supply the energy source for LED light with 10 minutes.

Contribution statement

Ms Y. Wang prepared most samples, executed the electrochemical measurements and analysed all data, Dr X. Zhang and Ms H. Wei obtained the SEM images, Mr X. Li obtained TEM images, Ms Y. Liu measured the XRD patterns, Ms X. Wang and Mr X. Liu measured the elemental mapping images and HRTEM images, Dr J. Xu and Dr W. Li measured the BET data, Mr Y. Liu prepared iron oxide sample, Ms Y. Wang, Dr M. Liang and Dr P. Jiang co-wrote the manuscript, Dr Liang and Dr Jiang co-designed the experiments.

Conflicts of interest

There are no conflicts to declare.

Acknowledgements

This work is supported by Beijing Municipal Science and Technology Project (No. Z161100001116080), National Key Scientific Instrument and Equipment Development Projects (No. 2014YQ090709), NSFC (21673273, 21103030), and Major Project of the Ministry of Science and Technology (No. 2016YFA0200904).

Notes and references

1 L. Dong, C. Xu, Y. Li, Z.-H. Huang, F. Kang, Q.-H. Yang and X. Zhao, *J. Mater. Chem. A*, 2016, **4**, 4659–4685.
2 X. Liu, Z. Wu and Y. Yin, *Chem. Eng. J.*, 2017, **323**, 330–339.
3 D. P. Dubal, O. Ayyad, V. Ruiz and P. Gomez-Romero, *Chem. Soc. Rev.*, 2015, **44**, 1777–1790.
4 M. Gao, L. Li and Y. Song, *J. Mater. Chem. C*, 2017, **5**, 2971–2993.
5 L. Kou, T. Q. Huang, B. N. Zheng, Y. Han, X. L. Zhao, K. Gopalsamy, H. Y. Sun and C. Gao, *Nat. Commun.*, 2014, **5**, 10.
6 Y. Zhang, Y. Zhao, X. L. Cheng, W. Weng, J. Ren, X. Fang, Y. S. Jiang, P. N. Chen, Z. T. Zhang, Y. G. Wang and H. S. Peng, *Angew. Chem., Int. Ed.*, 2015, **54**, 11177–11182.
7 J. Wang, S. Y. Dong, B. Ding, Y. Wang, X. D. Hao, H. Dou, Y. Y. Xia and X. G. Zhang, *Natl. Sci. Rev.*, 2017, **4**, 71–90.
8 Q. Zhu, K. Liu, J. Zhou, H. Hu, W. Chen and Y. Yu, *Chem. Eng. J.*, 2017, **321**, 554–563.
9 Y. Huang, H. Cheng, D. Shu, J. Zhong, X. Song, Z. Guo, A. Gao, J. Hao, C. He and F. Yi, *Chem. Eng. J.*, 2017, **320**, 634–643.
10 Q. Ke, M. Zheng, H. Liu, C. Guan, L. Mao and J. Wang, *Sci. Rep.*, 2015, **5**, 13940.
11 Y. Zhao, L. Hu, S. Zhao and L. Wu, *Adv. Funct. Mater.*, 2016, **26**, 4085–4093.
12 B. Shen, X. Zhang, R. Guo, J. Lang, J. Chen and X. Yan, *J. Mater. Chem. A*, 2016, **4**, 8180–8189.
13 C. Zhang, T. M. Higgins, S.-H. Park, S. E. O'Brien, D. Long, J. Coleman and V. Nicolosi, *Nano Energy*, 2016, **28**, 495–505.
14 F. Wang, S. Xiao, Y. Hou, C. Hu, L. Liu and Y. Wu, *RSC Adv.*, 2013, **3**, 13059–13084.
15 L. Aguilera, Y. Leyet, R. Peña-Garcia, E. Padrón-Hernández, R. R. Passos and L. A. Pocrifka, *Chem. Phys. Lett.*, 2017, **677**, 75–79.
16 B. Dong, M. Li, S. Chen, D. Ding, W. Wei, G. Gao and S. Ding, *ACS Appl. Mater. Interfaces*, 2017, **9**, 17890–17896.
17 D. S. Hall, D. J. Lockwood, C. Bock and B. R. MacDougall, *Proc. R. Soc. A*, 2015, **471**, 20140792.
18 Y. Wang, X. F. Zhang, X. Li, X. J. Li, Y. Zhao, H. Wei, Y. G. Liu, P. Jiang and M. H. Liang, *J. Colloid Interface Sci.*, 2017, **490**, 252–258.
19 N. Choudhary, C. Li, J. Moore, N. Nagaiah, L. Zhai, Y. Jung and J. Thomas, *Adv. Mater.*, 2017, **29**, 1605336.
20 N. Jabeen, A. Hussain, Q. Xia, S. Sun, J. Zhu and H. Xia, *Adv. Mater.*, 2017, **29**, 1700804.
21 A. Singh and A. Chandra, *Sci. Rep.*, 2015, **5**, 12.
22 Z. Zhang, H. Wang, Y. Zhang, X. Mu, B. Huang, J. Du, J. Zhou, X. Pan and E. Xie, *Chem. Eng. J.*, 2017, **325**, 221–228.
23 J. Sun, C. Wu, X. Sun, H. Hu, C. Zhi, L. Hou and C. Yuan, *J. Mater. Chem. A*, 2017, **5**, 9443–9464.
24 Z. H. Liu, X. C. Tian, X. Xu, L. He, M. Y. Yan, C. H. Han, Y. Li, W. Yang and L. Q. Mai, *Nano Res.*, 2017, **10**, 2471–2481.
25 L. B. Wang, H. L. Yang, X. X. Liu, R. Zeng, M. Li, Y. H. Huang and X. L. Hu, *Angew. Chem., Int. Ed.*, 2017, **56**, 1105–1110.
26 Y. Li, J. Xu, T. Feng, Q. F. Yao, J. P. Xie and H. Xia, *Adv. Funct. Mater.*, 2017, **27**, 10.
27 S. Zhang, B. Yin, Z. Wang and F. Peter, *Chem. Eng. J.*, 2016, **306**, 193–203.
28 X. Zheng, X. Yan, Y. Sun, Y. Yu, G. Zhang, Y. Shen, Q. Liang, Q. Liao and Y. Zhang, *J. Colloid Interface Sci.*, 2016, **466**, 291–296.
29 H. Quan, B. Cheng, Y. Xiao and S. Lei, *Chem. Eng. J.*, 2016, **286**, 165–173.
30 S. Deabate, F. Henn, S. Devautour and J. C. Giuntini, *J. Electrochem. Soc.*, 2003, **150**, J23–J31.
31 Y. Jiao, Y. Liu, B. Yin, S. Zhang, F. Qu and X. Wu, *Nano Energy*, 2014, **10**, 90–98.
32 W. Tian, X. Wang, C. Zhi, T. Zhai, D. Liu, C. Zhang, D. Golberg and Y. Bando, *Nano Energy*, 2013, **2**, 754–763.
33 Z. Li, W. Zhang, Y. Su, Z. Li and J. Groeper, *Nanotechnology*, 2017, **28**, 045603.
34 Y. Gao, D. L. Wu, T. Wang, D. Z. Jia, W. Xia, Y. Lv, Y. L. Cao, Y. Y. Tan and P. G. Liu, *Electrochim. Acta*, 2016, **191**, 275–283.
35 H. Zhang, Q. M. Gao, K. Yang, Y. L. Tan, W. Q. Tian, L. H. Zhu, Z. Y. Li and C. X. Yang, *J. Mater. Chem. A*, 2015, **3**, 22005–22011.
36 M. H. Liang, X. D. Wang, H. Q. Liu, H. C. Liu and Y. Wang, *J. Catal.*, 2008, **255**, 335–342.
37 C. Xiao, M. H. Liang, A. Gao, J. L. Xie, Y. Wang and H. C. Liu, *J. Nanopart. Res.*, 2013, **15**, 11.
38 H. Q. Liu, M. H. Liang, C. Xiao, N. Zheng, X. H. Feng, Y. Liu, J. L. Xie and Y. Wang, *J. Mol. Catal. A: Chem.*, 2009, **308**, 79–86.
39 X. Li, Y. Wang, L. Q. Li, W. Q. Huang, Z. C. Xiao, P. F. Wu, W. B. Zhao, W. Guo, P. Jiang and M. H. Liang, *J. Mater. Chem. A*, 2017, **5**, 11294–11300.
40 Y. Zhao, Y. N. Meng, H. P. Wu, Y. Wang, Z. X. Wei, X. J. Li and P. Jiang, *RSC Adv.*, 2015, **5**, 90307–90312.
41 M. Freitas, R. Silva, D. M. Anjos, A. Rozario and P. G. Manoel, *J. Power Sources*, 2007, **165**, 916–921.
42 L. Badr and R. Sultan, *Chem. Phys. Lett.*, 2008, **453**, 40–44.
43 X. Hu, S. Liu, C. Li, J. Huang, J. Luv, P. Xu, J. Liu and X.-Z. You, *Nanoscale*, 2016, **8**, 11797–11802.
44 X. F. Lu, X. Y. Chen, W. Zhou, Y. X. Tong and G. R. Li, *ACS Appl. Mater. Interfaces*, 2015, **7**, 14843–14850.
45 H. Jiang, H. Ma, Y. Jin, L. Wang, F. Gao and Q. Lu, *Sci. Rep.*, 2016, **6**, 31751.
46 R. Yang and L. Gao, *J. Colloid Interface Sci.*, 2006, **297**, 134–137.

47 L. Liu, J. Wang, C. Wang and G. Wang, *Appl. Surf. Sci.*, 2016, **390**, 303–310.
48 C. Zhao, X. Shao, Y. Zhang and X. Qian, *ACS Appl. Mater. Interfaces*, 2016, **8**, 30133–30142.
49 H. T. Zhang, X. Zhang, D. C. Zhang, X. Z. Sun, H. Lin, C. H. Wang and Y. W. Ma, *J. Phys. Chem. B*, 2013, **117**, 1616–1627.
50 Y. Miao, L. Ouyang, S. Zhou, L. Xu, Z. Yang, M. Xiao and R. Ouyang, *Biosens. Bioelectron.*, 2014, **53**, 428–439.
51 H. Yi, H. Wang, Y. Jing, T. Peng, Y. Wang, J. Guo, Q. He, Z. Guo and X. Wang, *J. Mater. Chem. A*, 2015, **3**, 19545–19555.
52 J. Li, F. L. Luo, X. Q. Tian, Y. Lei, H. Y. Yuan and D. Xiao, *J. Power Sources*, 2013, **243**, 721–727.
53 K. X. Li, Y. H. Luo, Z. X. Yu, M. H. Deng, D. M. Li and Q. B. Meng, *Electrochem. Commun.*, 2009, **11**, 1346–1349.
54 T. N. Murakami, S. Ito, Q. Wang, M. K. Nazeeruddin, T. Bessho, I. Cesar, P. Liska, R. Humphry-Baker, P. Comte, P. Pechy and M. Gratzel, *J. Electrochem. Soc.*, 2006, **153**, A2255–A2261.
55 X. Bai, Q. Liu, J. Liu, H. Zhang, Z. Li, X. Jing, P. Liu, J. Wang and R. Li, *Chem. Eng. J.*, 2017, **315**, 35–45.
56 J. J. Shen, X. C. Li, L. Wan, K. Liang, B. K. Tay, L. B. Kong and X. B. Yan, *ACS Appl. Mater. Interfaces*, 2017, **9**, 668–676.